Synthesis, Characterization, and Application of TiO₂ Nanoparticles – Effect of pH Adjusted Solvent

Ekemena Oghenovoh Oseghe, Patrick Gathura Ndungu, Sreekanth Babu Jonnalagadda*

School of Chemistry and Physics, University of Kwa-Zulu Natal, Westville Campus, Private Bag X 54001, Durban, 4000, South Africa

Abstract:

 TiO_2 nanoparticles were synthesized via the sol-gel method by varying the pH of the solvent used in the synthesis. The aim of the pH variation was to study its effect on the surface energy amongst other characteristics, and photocatalytic properties. The sol-gel method was adopted in the synthesis of TiO_2 nanoparticles and calcined in air at 400 °C at 2 °C/min. The as-prepared materials were characterized by X-ray powder diffraction (XRD), scanning electron microscopy (SEM), high resolution transmission electron microscopy (HRTEM), N_2 sorption, Raman spectroscopy, fluorescence spectrometry, and electron spin resonance spectroscopy (ESR), surface energy analyser (SEA), vibrating sample magnetometer (VSM). Photocatalytic properties of the materials were evaluated by monitoring the decoloration of model dye, methylene blue (MB) under natural sunlight conditions. The as-prepared materials existed in the anatase phase with polycrystalline and paramagnetic properties. The amount of surface defects of the as-prepared materials correlated well with the crystal size. The highest dispersive surface energy, 89.17 mJ/m² exhibited by TB400, and the least dispersive energy of 49.67 mJ/m² by TN400 are attributed to their microporosity. The acid - base numbers show that the materials are amphoteric with more of the basic sites. The values of the acidity-basicity ratio confirm the effect of pH in the synthesis of TiO_2 . The photocatalytic activities of the as-prepared materials were in the order of TB400 > TN400 > TA400, attributed to their characteristic crystal sizes, and surface defects.

Keywords: TiO₂ nanoparticle, surface energy, pH variation, photocatalysis

Introduction

Titania, a well-known semiconductor due to its unique physicochemical properties - stability of its chemical structure, biocompatibility, physical, optical, and electrical properties, is widely used in many applications (1). Its application in the area of catalysis, energy conversion, separation, sensors and other areas of nanotechnology are well recorded (2-4). The surface chemistry of TiO₂ has attracted special attention, since many physical and chemical processes, such as adsorption, transfer of photoexcited electrons to molecules, and desorption of product molecules, occurs on its surface (2, 5). Crystal facets in different orientation of TiO₂ are pivotal to its surface geometry and electronic structures, invariably leading to various physical and chemical properties (6).

Several synthetic routes in a bid to improve the surface properties of TiO₂ have been explored. These include the hydrothermal, microwave, sonochemical, electrodeposition, chemical vapour deposition (CVD), chemical solution decomposition, and the sol-gel method (2, 6-9). Since the sol-gel method facilitates the synthesis of nano-sized crystallized TiO₂ of high

purity at relatively low temperature (10), it has gained popularity in the synthesis of both doped and undoped TiO₂ (6). It involves the formation of colloidal suspension resulting from the hydrolysis and polymerization of the precursor (2).

Titania suffers fast hydrolysis and condensation process resulting most times in poorly structured and non-porous materials (11). In recent times, acid (low pH) has been used in slowing down this process for better structured materials (11, 12) but have never considered its effect on surface free energy. Surface free energy of materials plays a vital role in understanding its adhesion/interfacial interaction properties. The interfacial interaction property for catalysts and adsorbent surfaces defines their catalytic and adsorptive properties (13). Surface free energy is also important in explaining particle agglomeration phenomena, interactions between particles and adhesives, wetting phenomena, and the behavior of particles dispersed in liquids (14). It is therefore important that the surface chemistry of materials are understood as a guide to applications.

Inverse gas chromatography (IGC) is useful in understanding the performance of materials in applications and its surface chemistry (15). It is used

to study the surface energy of particulates, porous and fibrous materials (14, 15). Surface energy consists of dispersive, γ_S^D and polar or specific, γ_S^{SP} component caused by non-polar (Van der Waals force) and polar (acid-base) interactions respectively (16). The dispersive component of surface energy due to its high sensitivity is considered an important parameter for measurement in porous materials (15). The aim of this study was to measure the dispersive component and Lewis acid-base number of TiO_2 synthesized in different pH medium. The photocatalytic performance of the materials with methylene blue (MB) under sunlight was also studied.

Materials and Methods

For the synthesis of the photo-catalytic materials, we adapted a sol-gel technique that was initially developed by Aman et al., (12) and Ismail and Bahnemann (2). Titanium (IV) isopropoxide (TIP), purchased from Sigma-Aldrich (MW = 284.22, 97%) was used as TiO₂ precursor. The structure directing agent was a non-ionic surfactant (Pluronic F-127, Sigma-Aldrich), and the solvent used consisted of a mixture of 1-propanol (Sigma-Aldrich, HPLC grade) and ultra-pure water (1: 2.5 by volume). To synthesize the various samples, 50 mL of ultra-pure water was mixed with a few drops of either 0.1 M HNO₃ or 0.1 M NaOH to adjust the pH to values of 2, 7, or 11. Then 2.5 g of the surfactant was dissolved in 10 mL of 1-propanol, and then added to the pH adjusted water and allowed to stir for 10 minutes. 5 g of the titanium isopropoxide was then mixed with 10 mL of 1propanol, and then added slowly drop by drop to the surfactant solvent mixture. After approximately 4.0 hours, the solutions were centrifuged and the precipitates recovered. The samples were placed in an alumina boat and transferred to a horizontally aligned tube furnace. Samples were then dried at 100 °C (4.0 hours), and then heat treated at 200 °C for 1h and finally calcined at 400 °C for 4 hours (ramp rate from 200 °C – 400 °C was 2 °C/min). The resulting samples were marked as TA400, TB400, TN400, where T = Titanium, A = acidic condition (pH = 2), B = basiccondition (pH = 11), N = neutral (pH = 7), and 400 = calcination temperature in Celsius.

Catalyst Characterization

The surface morphology of the materials was examined on a Leo 1450 Scanning Electron Microscope equipped with energy dispersive X-ray analyser (EDX). Detailed physical structural characteristics were observed with a JEOL JEM-1010 transmission electron microscope (17). The phases of the materials were observed using powder X- ray diffraction (XRD)

conducted on a Bruker D8 Advance instrument, equipped with a XRK 900 reaction chamber, a TCU 750 temperature control unit and a Cu Kα radiation $(\lambda=0.15406 \text{ nm})$. The textural characteristics were determined by using a Micrometrics Tri-Star II 3030 instrument. Samples were degassed prior to textural analysis by using a Micrometrics Flow Prep (060) under N₂ flow at 90 °C for 1hr, and then increasing the temperature to 200 °C, and leaving the samples to de-gas for approximately 12 hours. UV-visible diffuse reflectance spectra were recorded with an Ocean Optics high resolution spectrometer (HR2000+) equipped with an integrating sphere accessory, using BaSO₄ as a reference. Infrared spectra of the samples were recorded using Fourier transmission infrared (FTIR) spectrometer (PerkinElmer spectrum 100 series with universal ATR accessory). EPR data was collected at room temperature on a microwave resonator of a Bruker EMX-plus X-band ESR spectrometer. Data acquisition: frequency, 9.853713 GHz; power, 2.00 mW; modulation amplitude, 2.00 G (modulation frequency 100.00 kHz); time constant, 81.92 ms; conversion time, 18.00 ms; sweep width, 2500 G (Centre field=3500 G); data resolution, 5000 points.

Photoluminescence spectroscopic study of the materials was performed on a Perkin Elmer LS 55 fluorescence spectrophotometer, where the samples were excited with higher photon energy (310 nm). LakeShore model 735 vibrating sample magnetometer (VSM) was used to obtain the magnetic properties of the samples. The instrument was calibrated with a standard Ni sphere of saturation magnetization 54.7 emu g⁻¹ prior to sample analysis. The analysis was carried out at room temperature with a maximum applied magnetic field of 14 kOe. Dispersive energy and surface acidity/basicity of the materials were performed on a new generation IGC (Surface energy analyser (SEA)). A range of dispersive probes; pentane, hexane, heptane, octane, and nonane were injected with fractional surface coverage of 5% in order to determine the concentration of free dispersive energy. Polar probes such as ethyl acetate, dichloromethane, acetonitrile, were also analyzed with the same fractional surface coverage as with the dispersive probes. The column dead volume was obtained using methane (inert probe) with injection volume of 0.2 mL. The dispersive component was obtained using the Doris and Gray approach and the polar components obtained using the Schultz approach.

Photocatalytic Tests

Photocatalytic properties of the materials were tested on methylene blue (MB) as a model dye. The

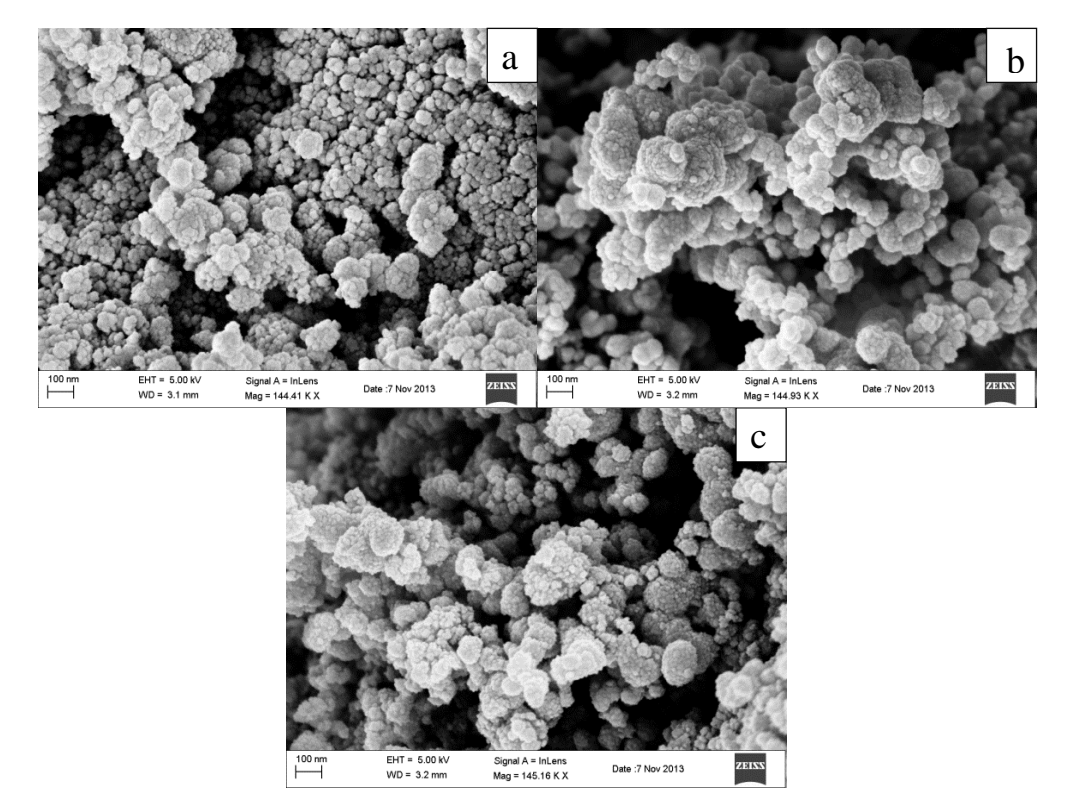


Figure 1. SEM micrograph of (a) TA400, (b) TB400, and (c) TN400

test was carried out in a simple open quartz photochemical reactor under natural sunlight. Prior to light irradiation, 0.1 g of the photocatalyst was added to 200 mL of MB (5 mg/L) aqueous solution of pH 5.8, and then the mixture was sonicated in an ultrasound bath (Selectech (PTY) LTD, UMC20, 400 W, 20 L)), for 10 minutes, to disperse the powder. The mixture was then kept in the dark for 1 hr, under continuous stirring in order to attain adsorption-desorption equilibrium. The photocatalytic experiment was done during summer in the month of October 2013. The experimental temperature, solar power and UV had an average value of 28 °C, 1121.25 W/m², and 116.58 W/m² respectively as measured by solar irradiance meter (TM-208). At given time intervals (20 min), 1.0 mL aliquots were taken from the solution and immediately centrifuged at 14000 r/min, the solution decanted, and the absorbance recorded on a UV-Visible spectrometer (Libra S6) at 665 nm. The determined absorbance was converted to concentration by using a calibration curve constructed from known concentrations of MB.

Results and Discussion *Morphology*

SEM and HRTEM micrographs (fig. 1 and 2 respectively) were collected in order to evaluate the surface morphology and crystallinity of the materials.

The SEM micrographs show that all the materials consist of irregular and spherically shaped aggregates of agglomerated particles ranging from 47-100 nm in size, with inter-particle voids. TB400 showed higher level of agglomeration, while TA400 exhibited the least. The characteristic agglomeration of TA400 may be due to peptization effect at lower pH (1, 18). HRTEM images also validate SEM micrograph as regards agglomerates between the particles. It reveals uniform lattice fringes with spacing corresponding to (101) planes (d-spacing ≈ 0.35 nm) of the anatase phase of TiO₂. The selected area electron diffraction pattern (insert of fig. 2) confirms the polycrystalline characteristics of the materials.

Textural Characteristics

Figure 3 represents the N_2 sorption isotherms and pore size distribution curves of TiO_2 samples of different pH. BET surface area, pore volume, pore diameter, and particle size are summarized in Table 1. According to IUPAC classification, the isotherms are identified as type IV with the H1 hysteresis loop suggesting a mesoporous structure of the materials, with narrow pore size distribution (insert) (19). The hysteresis loop observed at high relative pressure, is associated with the capillary condensation occurring in the mesopores, signifying the dominance of uniform large pores (20). The pore size distribution as obtained

Table 1. Textural and structural Characteristics of the materials

Samples	Surface area (m²/g)	BET Average Pore diameter (nm)	Pore volume (cm³/g)	Average particle size (nm)	Anatase Crystallite size (nm)	Lattice parameter (A°)	Unit cell volume (A°) ³
TB400	52.15	11.74	0.15	115.3	6.6	a = b = 3.791 c = 9.487	136.35
TN400	59.76	10.10	0.15	100.4	7.3	a = b = 3.793 c = 9.502	136.73
TA400	49.02	11.90	0.13	122.4	8.5	a = b = 3.789 c = 9.487	136.26

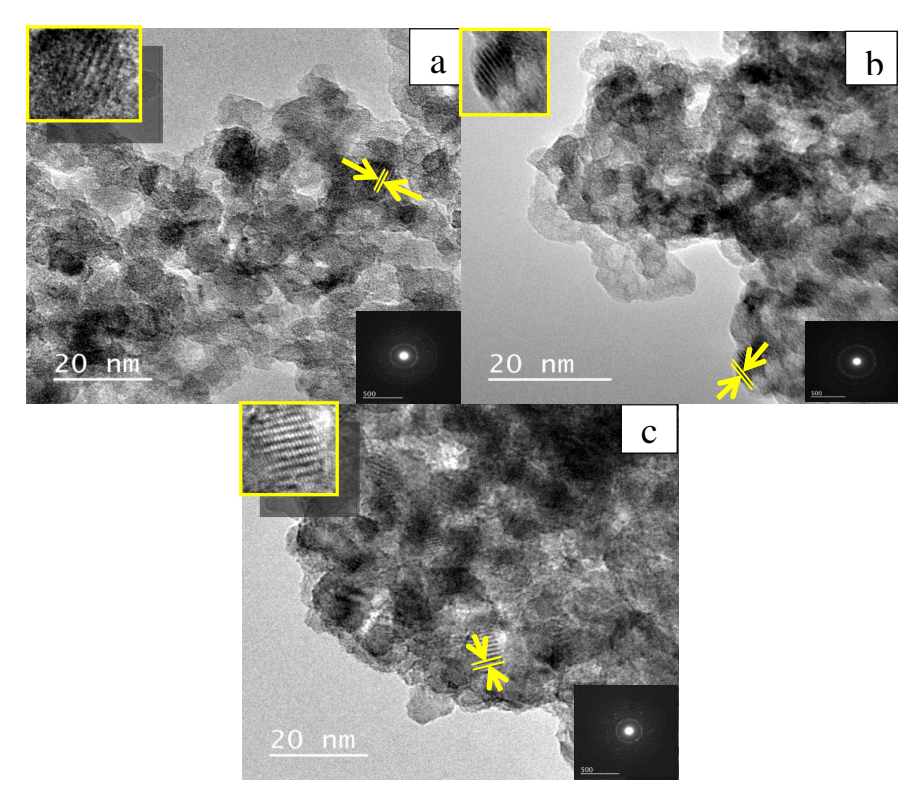


Figure 2. HRTEM micrograph (a) TA400, (b) TB400, and TN400 with inserts showing lattice fringes and diffraction pattern.

from the BJH desorption curves of the different TiO_2 , ranges from 3.23 - 6.33 nm, with TA400 been distributed at 3.23 and 6.33 nm.

XRD- Structural Analysis

Phase identification, Scherer's crystal size, lattice parameters were determined by x-ray diffraction (figure 4). All the samples show broad peaks at around $2\theta = 25.3$ (101); 37.9 (004); and 47.9 (200), which corresponds to the anatase phase of titania according to the JCPDS file no. 21-1272. The broad peaks are characteristics of nano-sized materials.

The average crystallite size (D) was estimated with Scherer's equation.

$$D = \frac{\kappa\lambda}{\beta\cos\theta} \tag{1}$$

where k is a constant (dependent on crystal shape \approx 0.9), λ is the X-ray wavelength (0.15418 nm), β is the full width at half maximum (FWHM) of the diffraction peak, and θ is the diffraction angle. The values of β and θ are taken for the crystal plane (101) of anatase phase. The crystallite sizes of the materials are shown in table 1. TB400 had the smallest crystallite size while TA400 exhibited a larger crystallite size; which implies that the synthesis of TiO₂ under basic condition inhibits the anatase grain growth more than other pH conditions.

The X-ray diffraction peaks of crystal plane (200) and (004) of anatase were selected to determine the lattice parameter of the materials. The lattice parameters are obtained by using the following equations: Bragg's equation,

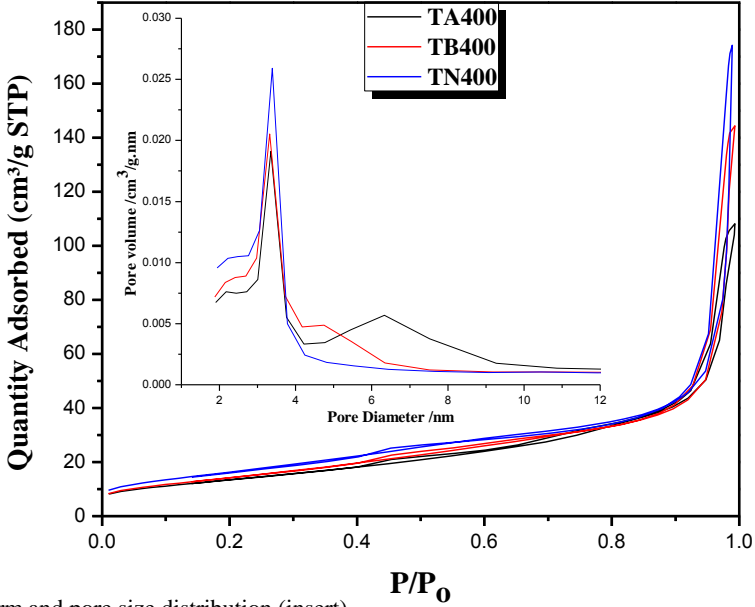


Figure 3. N₂ sorption isotherm and pore size distribution (insert).

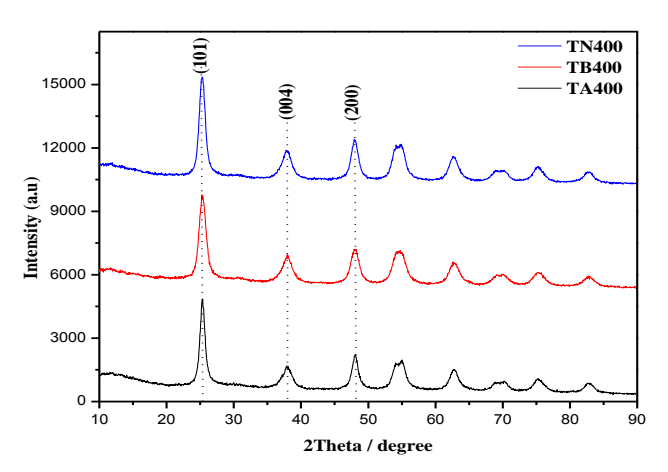


Figure 4. X-ray diffractogram of the materials.

$$n\lambda = 2d \sin\theta \tag{2}$$

$$\frac{1}{d^2} = \frac{h^2 + k^2}{a^2} + \frac{l^2}{c^2} \tag{3}$$

where n is an integer, θ is the angle between the incident ray and the scattering planes of (hkl), d is the distance between crystal planes of (hkl), λ is the wavelength of X-ray used, hkl is the crystal plane indices and a, and c are lattice parameters (in the anatase phase $a = b \neq c$). The lattice parameters and the unit cell volume of all the samples are shown in Table 1. Anatase contains four TiO₂ molecules per unit cell having lattice parameters of a = 3.78 Å and c = 9.51 Å (5).

Raman Spectroscopy

Figure 5 shows the Raman spectra for TiO₂ synthesized at different pH conditions. They all exhibit well-defined Raman modes around 200, 398, 520, and

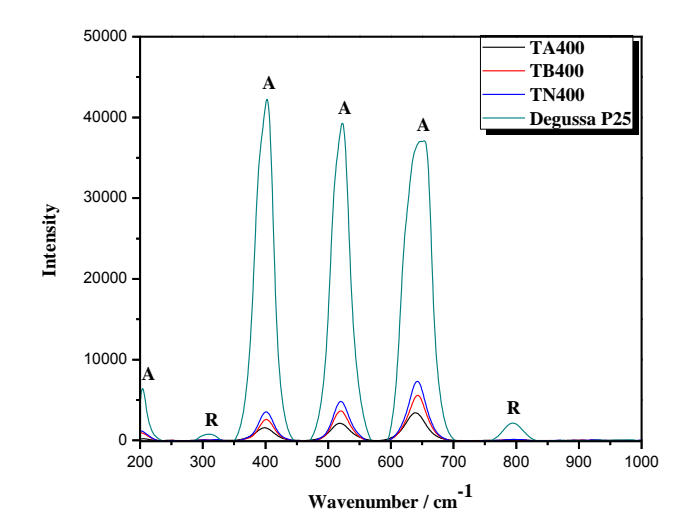


Figure 5. Raman spectra of the materials.

642 cm⁻¹, characteristic mode for anatase phase. According to factor group analysis, anatase has six Raman active modes (A1g + 2B1g + 3Eg). Ohsaka reported the Raman spectrum of an anatase single crystal that the six allowed modes appears at 144 cm⁻¹ (Eg), 197 cm⁻¹ (Eg), 399 cm⁻¹ (B1g), 513 cm⁻¹ (A1g), 519 cm⁻¹ (B1g), and 639 cm⁻¹ (Eg) (21). The benchmark, Degussa P25, exists in two phases – 20% rutile and 80% anatase. The bands appearing at 216 and 687 cm⁻¹, with P25, are attributed to the rutile phase. This tie into the XRD results on the phase of the materials.

FT-IR Spectroscopy

The FT-IR spectra of the benchmark TiO₂ (Degussa P25), and TiO₂ synthesized with different pH water is presented in Figure 6.

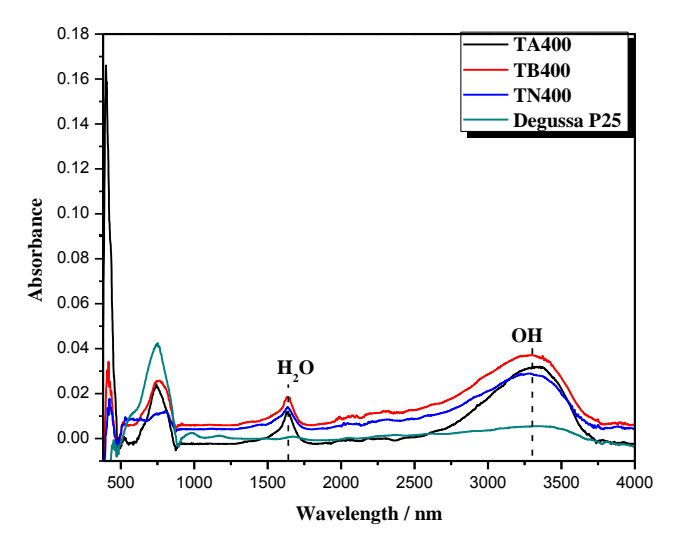


Figure 6. FTIR sprectra for the materials.

The wide bands at 3269-3304 cm⁻¹ and around 1630 cm⁻¹, are mainly ascribed to the presence of the surface adsorbed OH and H₂O groups respectively. In an increasing order (Degussa P25 < TN400 < TA400 < TB400), the intensity of absorption band of surface adsorbed OH at around 3269-3304 cm⁻¹ increased. The highest absorbance intensity of the surface OH group exhibited by TB400 might be due to the basic precursor (NaOH) used in attaining pH, 11, of the water used for synthesis. The hydroxyl group on the surface of semiconductors are vital in photocatalytic applications since they can capture photoinduced holes from the surface of materials, inhibiting electron-hole recombination as well as forming hydroxyl radicals with high oxidation potential (22, 23). Signals between 400 and 1000 cm⁻¹ corresponds to Ti-O-Ti vibration (24).

Optical Characteristics of TiO₂

The optical absorption spectra of Degussa P25 and TiO_2 synthesized at pH = 2, 7, and 11 by a UV– Vis spectrometer in the range of 320-900 nm are presented in Figure 7. Intense absorptions were observed in the wavelength range of about 330-395 nm. TiO_2 at different pH conditions of synthesis, when compared with the benchmark, Degussa P25, exhibited red shifts, which implies less band gap energies. The red shift are in the order of TN400 < TB400 < TA400, correlating with their average particle sizes (table 1) (25).

The direct band gap energy was estimated by Tauc plot (figure 7 (insert)) following equation 4.

$$(\alpha h v)^2 = A(hv - E_g)$$
 (4)

where hv = photon energy, α = absorption coefficient ($\alpha = 4\pi k/\lambda$; $\pi = 3.142$, k is the absorption index or

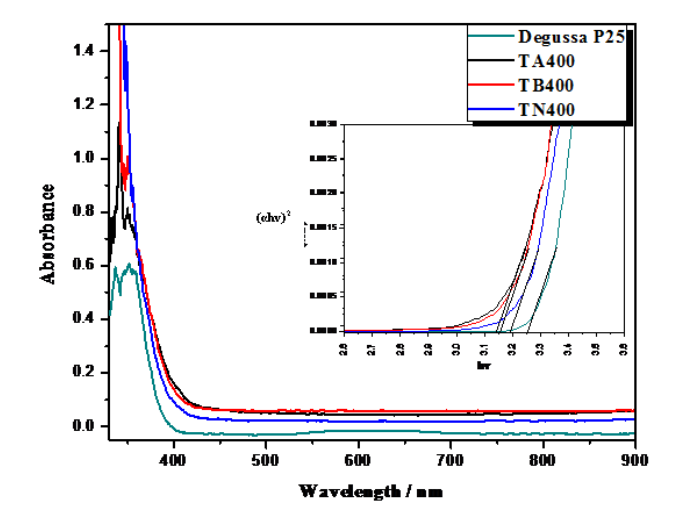


Figure 7. UV-DRS of the materials and Tauc plot (insert).

absorbance, and λ is the wavelength in nm), Eg = energy band gap, A = constant. The value of band gap was determined by extrapolating the straight line portion of $(\alpha hv)^2$ on hv axis as shown in the insert of Figure 7 (5). Approximate direct band gap energies of the samples are obtained from the intercept of the tangent to the curves. The band gap decreases as the particle sizes increased; with TA400 of the synthesized TiO₂ having the least band gap energy of 3.14 eV and TN400 has the highest of about 3.19 eV (25). The characteristic band gap energies exhibited by the samples corroborates the XRD results (fig. 7), with regards to the phase (anatase, 3.20 eV) (17).

In order to expatiate on the optical characteristics of the materials, photoluminescence spectroscopic experiment was done. Figure 8 shows the PL spectra of Degussa P25 and TiO₂ synthesized in different pH medium. Band emissions were observed at 403, 421, 425, 441, 446, 460, 466, 484, and 528 nm which are in accordance with band emissions obtained by Tripathi et al. (25). According to Tripathi et al. (25), PL spectra of anatase TiO₂ are attributed to self-trapped excitons, oxygen vacancies, and surface states. Band edge emissions of 376, 378, and 382 nm can be attributed to excitons recombination (25), 485 nm bands can be ascribed to self-trapped excitons localized on TiO₆ octahedral (26), and PL bands at longer wavelength side of TiO₂ nanoparticles are assigned to the oxygen vacancies (25-27). According to Zhu et al. (28), detecting exciton emission with bulk TiO₂ by fluorescence spectrophotometry at room temperature is impossible. This is a result of its weak exciton binding energy and short radiative lifetime. However, findings from Takagahara and Takeda (29) show that the exciton binding energy and radiative lifetime are strongly dependent on size. A decrease in

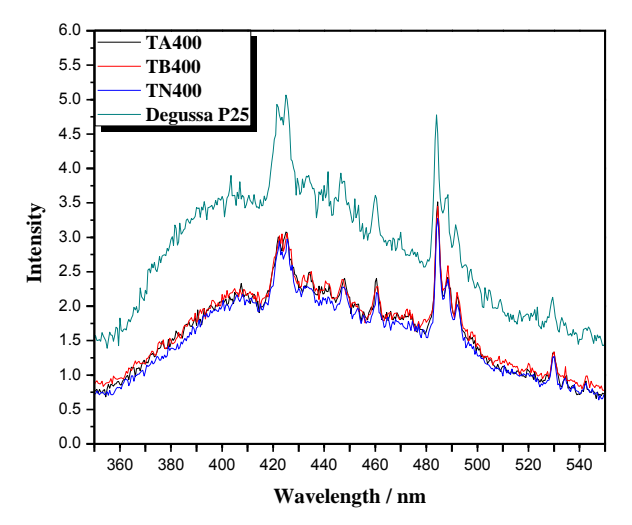


Figure 8. Photoluminescence spectra for degussa P25 and the synthesized TiO_2 .

the size of the semiconductor quantum dots, leads to a corresponding increase in the spatial overlap of the envelope functions of an electron and hole. This leads to an increase in the binding energy which invariably prolongs the exciton radiative lifetime. Also, the dielectric confinement effect which also enhances the exciton binding energy becomes stronger in TiO₂ particles with smaller quantum dots (30). This suggests that both the as-prepared TiO₂ and Degussa P25 possesses large exciton binding energies, hence, a long exciton radiative lifetime, which leads to the photoluminescence of the Wannier—Mott free exciton which is observed by ordinary fluorescence spectrophotometry at room temperature.

A decrease in emission intensity of TiO₂ might be due to an introduction of new defect sites that enhances non-radiative recombination of the excited electron (5, 31) or the presence of a single phase which is mostly anatase (25). The PL spectra confirms XRD and Raman results of this study in terms of the phase of the synthesized TiO₂ since they all show less intensity when compared with Degussa P25 (20% rutile and 80% anatase). Of all synthesized TiO₂, TN400 has the least tendency of having rutile phase when calcined at a higher, and enhanced non-radiative recombination of excited electrons.

Magnetic Properties

Figure 9 shows the signals of the materials obtained from the ESR experiment. These signals confirms that the materials are paramagnetic with major g-factor appearing at ≈ 1.99 for all materials and Degussa P25 having other g-factors of 1.9671 and 1.9346 (Table 2). Sa et al. (32), ascribed signal with a g-factor of 1.993 to the Ti^{3+} species of anatase and g-factor of 1.970 and 1.951 attributed to Ti^{3+} of the

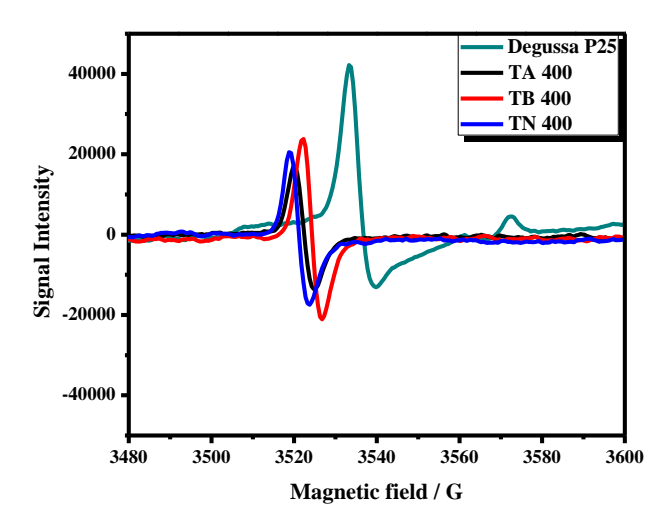


Figure 9. ESR spectra of TiO2 synthesized using different pH media.

rutile phase. Kongsuebchart et al. (33) assigned signals at g-factor of 1.996 to Ti^{3+} species on the surface of TiO_2 . In this work, signals that appeared at g-factor of ≈ 1.99 can be attributed to the surface Ti^{3+} species since the intensity of signals of the asprepared materials varies with change in pH. The amount of surface defects of the as-prepared materials correlates with the crystal size of the anatase (Table 1) obtained from the diffractogram of the as-prepared materials, TB400 showed highest surface defect and TA400 showed the least surface defect. This implies that TB400 would perform best in photocatalytic application (34-36).

The magnetic properties of the as-prepared materials and Degussa P25 were analyzed using vibrating sample magnetometer. These magnetic properties such as saturation magnetization (Ms), remnant magnetization (37) are presented in Table 2. Figure 10 shows that all samples exhibited paramagnetic properties, which confirm the results obtained from the ESR experiment. An increase in the paramagnetic behavior from TiO2 synthesized in acid media, TA400, to TiO₂ synthesized in basic media was also observed with TB400 of the as-prepared materials exhibiting the highest saturation magnetization of 1.1652 emu g⁻¹ and TA400 had the least saturation magnetization of 0.9042 emug⁻¹. Amongst the as-prepared TiO₂, the relatively highest saturation magnetization property displayed by TB400 is due to its highest amount of unpaired electrons as shown by the ESR experiment.

Dispersive Energy and Acid-base Properties of the Materials

The characteristic adsorption of the non-polar (n-alkane) probes on the materials was determined by the

Table 2. Paramagnetic properties obtained from ESR and VSM experiment

Samples	G factor	Ms/emug ⁻¹	Mr/emug ⁻¹		
Degussa P25	1.98877, 1.96706, 1.93456	1.2992	0.16963		
TB400	1.99719	1.1652	0.28121		
TN400	1.99691	1.0259	0.28282		
TA400	1.99706	0.9042	0.36024		

Table 3. Pseudo first-order kinetics of MB decoloration and surface energy of the materials

Photocatalyst(s)	Rate Constant	\mathbb{R}^2	Dispersive surface energy (D &G)	Acid – base parameters (Schultz)			
			(mJ/m^2)	K _A	K _B	K _A - K _B ratio	\mathbb{R}^2
MB alone	3.34×10 ⁻³	0.9000	-	-	-	-	-
TA 400	6.44×10^{-3}	0.9167	55.70	0.0627	0.5031	0.9611	0.9611
TN 400	9.20×10^{-3}	0.9573	49.67	0.0911	0.3197	0.2851	0.9952
TB 400	1.33×10 ⁻²	0.9511	89.17	0.0689	0.7401	0.0931	0.9026
Degussa P25	2.10×10^{-2}	0.9094	47.94	0.0564	0.3592	0.1571	0.9997

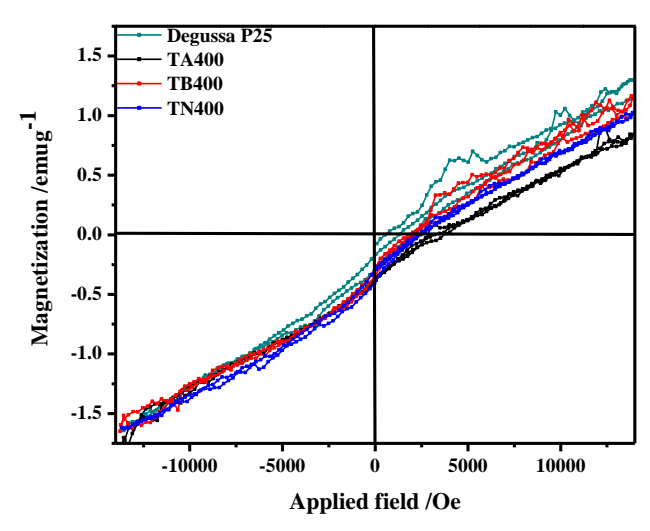


Figure 10. Magnetization curves of as-prepared and commercial TiO₂.

dispersive component of surface energy. The values of the dispersive surface energy, γ_S^D of the materials (5% surface coverage) at 40 °C are shown in Table 3. Material synthesized under basic condition, TB400, exhibited the highest dispersive surface energy of 89.17 mJ/m² while TN400 had the least dispersive energy of 49.67 mJ/m². The difference in the dispersive energies of the materials might be due to their microporosity (pore size distribution (insert of figure 3)) (38). The acid and base numbers (K_A and K_B , respectively) obtained from the interaction between the polar probes and the materials are shown in table 3. The acid - base parameters show that the

materials are amphoteric having more of the acidic sites $(K_B > K_A)$ that may have resulted from the solvents and surfactant used in their synthesis. A positive correlation was observed between the rate constant of MB decoloration and the number of acidic sites present in the materials. This correlates with the surface OH group present in the materials as presented in the FTIR spectra (figure 6). The hydroxyl group on the surface of a material acts as a bronsted acid and plays an important role in water-based photocatalytic reactions, since they can capture any photoinduced holes that make it to the surface of the material. This process inhibits electron-hole recombination, and fosters the formation hydroxyl radicals with high oxidation potentials (22, 23). The values of the acidity-basicity ratio in Table 3, confirms the effect of pH in the synthesis of TiO₂.

Photocatalytic Activities of the As-prepared Materials under Sunlight

The photocatalytic properties of the materials were investigated on 10 mg/L MB solution of natural pH of about 6.12 under sunlight. Figure 11 shows the photocatalytic activities under solar irradiation. After 100 min of irradiation, TB400 amongst the as-prepared materials showed highest photocatalytic characteristics while TA400 exhibited the least photocatalytic activities. The photocatalytic activities exhibited by the as-prepared materials could be attributed to their characteristic crystal sizes, and surface defects as shown in table 1 and figure 9 respectively (6, 34, 35).

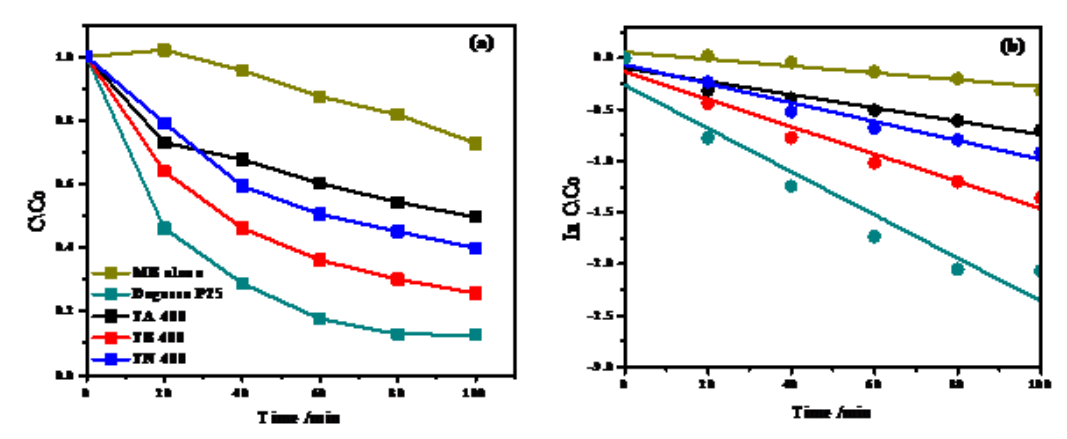


Figure 11. Photocatalytic activity (a) and pseudo first-order kinetics plot of MB decoloration by the materials.

The high photocatalytic activity exhibited by Degussa P25 might be due to the presence of the rutile phase and electron trapping site (39). The kinetics for the photocatalytic decoloration of MB by the as-prepared materials is presented in figure 11b with plots following the pseudo first-order kinetics. The apparent rate constant, $K_{\rm MB}$ obtained from the slope of the plots are presented in Table 3.

One of the key findings in terms of synthesis parameters used is that the basic sample TB400, had distinctly different physical-chemical characteristics, when compared to the other two samples. In terms of the textural characteristics the various synthesized samples are very similar, thus this cannot account for the differences in photo-catalytic activity. The smaller crystallite size with TB400 would imply greater trap sites at the grain boundaries within the particulates. In addition the band gap changes slightly between 3.14 – 3.19 eV for all the synthesized samples. In addition the PL spectra are very similar for each of the synthesized samples, but the intensity is less than that of the bench mark catalyst. However, the TB400 has the greatest catalytic rate compared to the other two synthesized samples and is lower than that of P25. The ESR measurements provided evidence for the presence of Ti³⁺ within all the samples, and the magnetic measurements showed that the TB400 sample has a greater saturation n magnetization due to larger amounts of unpaired electrons and hence more Ti³⁺. This correlates well with the dispersive surface energy, where recent reports in the literature have shown that larger surface energy values are due to under-coordinated Ti sites on the surface of the particles (40). The photo-catalysts generate electron hole pairs when excited by UV-Vis radiation, and these eventually form OH or oxygen radicals on the surface of the particles (41). The presence of a greater amount of Ti³⁺ will produce more oxygen radicals, an observation that was recently reported by Zhang et al.

(42). The commercial catalyst performs better in this system, since it favors production of OH radicals, which have been shown to be the likely and most effective pathway for degradation of methylene blue (41). Thus the synthesized catalysts would function in system where oxygen radicals have been shown to be advantageous, such as methylene orange (42), or with a system that can provide a more conducive source of oxygen radicals; specifically, ozone. The synthesized catalysts favor the formation of oxygen radicals, due to the relatively larger amounts of Ti³⁺, and thus the increased rate with the TB400 using ozone.

The tailoring of characteristics of titania via a simple pH mediated synthesis route could be advantageous in water treatment plants that already use ozone in the treatment stream, and may find the combination of ozone and modified titania beneficial in removing a wide range of organic pollutants.

Conclusions

TiO₂ nanoparticles were synthesized using deionized water adjusted to different pH values via the sol-gel method. The as-prepared materials exist in the anatase phase with polycrystalline characteristics. These materials exhibited paramagnetic properties with an increase in saturation magnetization as the pH tends towards basic. The amount of surface defects of the as-prepared materials correlates with the crystal size with TB400 showing highest surface defects while TA400 showed the least surface defect. TB400 exhibited the highest dispersive surface energy, 89.17 mJ/m², while TN400 had the least dispersive energy of 49.67 mJ/m² attributed to their microporosity. The acid - base numbers show that the materials are amphoteric having more of the basic sites. The values of the acidity-basicity ratio confirm the effect of pH in the synthesis of TiO₂. The photocatalytic activities exhibited by the as-prepared materials can be attributed to their characteristic crystal sizes, and surface defects.

The greater amount of Ti³⁺ within the prepared samples results in the photo-catalytic process producing oxygen radicals as opposed to OH radicals when compared to P25. Thus these catalysts are more suited to photo-ozonation processes, and maybe effective in degrading multiple organic pollutants in a single batch.

Acknowledgement

The authors appreciate iThemba LABS, Materials Research Department, and the School of Chemistry and Physics, University of KwaZulu-Natal, Westville Campus, Durban, South Africa for the financial support and research facilities.

References

- (1) Oskam, G.; Nellore, A.; Penn, R.L.; Searson, P.C. *Journal of Physical Chemistry B* **2003**, *107*, 1734-1738.
- (2) Ismail, A.A.; Bahnemann, D.W. *Journal of Materials Chemistry* **2011**, *21*, 11686-11707.
- (3) Admassie, S.; Inganas, O.; Mammo, W.; Perzon, E.; Andersson, M.R. *Synthetic Metals* **2006**, *156*, 614-623.
- (4) Kim, J.Y.; Noh, J.H.; Zhu, K.; Halverson, A.F.; Neale, N.R.; Park, S.; Hong, K.S.; Frank, A.J. *Acs Nano* **2011**, *5*, 2647-2656.
- (5) Chauhan, R.; Kumar, A.; Chaudhary, R.P. Spectrochimica Acta Part a-Molecular and Biomolecular Spectroscopy 2012, 98, 256-264.
- (6) Macwan, D.P.; Dave, P.N.; Chaturvedi, S. *Journal of Materials Science* **2011**, *46*, 3669-3686.
- (7) Ho, G.W.; Chua, K.J.; Siow, D.R. Chemical Engineering Journal **2012**, 181, 661-666.
- (8) Lin, H.C.; Su, C.Y.; Yang, Z.K.; Lin, C.K.; Ou, K.L. *Particuology* **2011**, *9*, 517-521.
- (9) Dong, X.; Zhang, F.; Hua, C.; Rong, C.; Zhang, X.; Ma, H.; Shi, F.; Zhang, X.; Ma, C.; Xue, M. J. Adv. Oxid. Technol. 2014, 17, 39-43.
- (10) Peng, F.; Cai, L.; Huang, L.; Yu, H.; Wang, H. Journal of Physics and Chemistry of Solids 2008, 69, 1657-1664.
- (11) Meynen, V.; Cool, P.; Vansant, E.F. *Microporous* and *Mesoporous Materials* **2009**, *125*, 170-223.
- (12) Aman, N.; Satapathy, P.K.; Mishra, T.; Mahato, M.; Das, N.N. *Materials Research Bulletin* **2012**, *47*, 179-183.
- (13) Zhang, X.; Shi, B.; Wang, Y. *Journal of Adhesion Science and Technology* **2012**, *26*, 353-360.
- (14) Yla-Maihaniemi, P.P.; Heng, J.Y.Y.; Thielmann, F.; Williams, D.R. *Langmuir* **2008**, *24*, 9551-9557.
- (15) Rueckriem, M.; Inayat, A.; Enke, D.; Glaeser, R.; Einicke, W.D.; Rockmann, R. *Colloids and Surfaces a-Physicochemical and Engineering Aspects* **2010**, 357, 21-26.

- (16) Gamble, J.F.; Leane, M.; Olusanmi, D.; Tobyn, M.; Supuk, E.; Khoo, J.; Naderi, M. *International Journal of Pharmaceutics* **2012**, 422, 238-244.
- (17) Asilturk, M.; Sener, S. Chemical Engineering Journal **2012**, 180, 354-363.
- (18) Vorkapic, D.; Matsoukas, T. *Journal of Colloid and Interface Science* **1999**, 214, 283-291.
- (19) Sing, K.S.W.; Everett, D.H.; Haul, R.A.W.; Moscou, L.; Pierotti, R.A.; Rouquerol, J.; Siemieniewska, T. *Pure and Applied Chemistry* **1985**, *57*, 603-619.
- (20) Lee, ; Orilall, J. M.C.; Warren, S.C.; Kamperman, M.; Disalvo, F.J.; Wiesner, U. *Nature Materials* **2008**, *7*, 222-228.
- (21) Ohsaka, T. Journal of the Physical Society of Japan 1980, 48, 1661-1668.
- (22) Hou, Y.D.; Wang, X.C.; Wu, L.; Chen, X.F.; Ding, Z.X.; Wang, X.X.; Fu, X.Z. *Chemosphere* **2008**, 72, 414-421.
- (23) Xu, Y.; Lei, B.; Guo, L.; Zhou, W.; Liu, Y. *Journal of Hazardous Materials* **2008**, *160*, 78-82.
- (24) Neumann, B.; Bogdanoff, P.; Tributsch, H.; Sakthivel, S.; Kisch, H. *Journal of Physical Chemistry B* **2005**, *109*, 16579-16586.
- (25) Tripathi, A.K.; Singh, M.K.; Mathpal, M.C.; Mishra, S.K.; Agarwal, A. *Journal of Alloys and Compounds* **2013**, *549*, 114-120.
- (26) Saraf, L.V.; Patil, S.I.; Ogale, S.B.; Sainkar, S.R.; Kshirsager, S.T. *International Journal of Modern Physics B* **1998**, *12*, 2635-2647.
- (27) Zeng, H.; Cai, W.; Liu, P.; Xu, X.; Zhou, H.; Klingshirn, C.; Kalt, H. Acs Nano 2008, 2, 1661-1670.
- (28) Zhu, Y.C.; Ding, C.X.; Ma, G.H.; Du, Z.L. *Journal of Solid State Chemistry* **1998**, *139*, 124-127.
- (29) Takagahara, T.; Takeda, K. *Physical Review B* **1992**, 46, 15578-15581.
- (30) Takagahara, T. Physical Review B 1993, 47, 4569-4585.
- (31) Zhang, S.; Zhao, Z.Y.; Liu, C.X.; Dong, W.; Zhang, X.D.; Chen, W.Y. *Journal of Materials Science* **2004**, *39*, 2909-2910.
- (32) Sa, J.; Fernandez-Garcia, M.; Anderson, J.A. *Catalysis Communications* **2008**, *9*, 1991-1995.
- (33) Kongsuebchart, W.; Praserthdam, P.; Panpranot, J.; Sirisuk, A.; Supphasrirongjaroen, P.; Satayaprasert, C. *Journal of Crystal Growth* **2006**, 297, 234-238.
- (34) Sirisuk, A.; Klansorn, E.; Praserthdam, P. *Catalysis Communications* **2008**, *9*, 1810-1814.
- (35) Suriye, K.; Praserthdam, P.; Jongsomjit, B. *Applied Surface Science* **2007**, 253, 3849-3855.
- (36) Gao, H.; Qiao, B.; Wang, T.J.; Wang, D.; Jin, Y. *Industrial & Engineering Chemistry Research* **2014**, 53, 189-197.

- (37) Poll, C.; Pagel, H.; Devers-Lamrani, M.; Martin-Laurent, F., Ingwersen, J.; Streck, T.; Kandeler, E. *Soil Biology & Biochemistry* **2010**, *42*, 1879-1887.
- (38) Swaminathan, V.; Cobb, J.; Saracovan, I. *International Journal of Pharmaceutics* **2006**, *312*, 158-165.
- (39) Tryba, B.; Toyoda, M.; Morawski, A.W.; Nonaka, R.; Inagaki, M. *Applied Catalysis B-Environmental* **2007**, *71*, 163-168.
- (40) Xu, H.; Reunchan, P.; Ouyang, S.; Tong, H.; Umezawa, N.; Kako, T.; Ye, J. *Chemistry of Materials*

- **2013**, 25, 405-411.
- (41) Ono, Y.; Rachi, T.; Okuda, T.; Yokouchi, M.; Kamimoto, Y.; Nakajima, A.; Okada, K. *Journal of Physics and Chemistry of Solids* **2012**, *73*, 343-349.
- (42) Mingyang, X.; Wenzhang, F.; Muhammad, N.; Yunfei, M.; Jinlong, Z.; Masakazu, A. *Journal of Catalysis* **2013**, 297, 236 243.

Received for review November 5, 2014. Revised manuscript received December 19, 2014. Accepted December 27, 2014.